

Embedded Mean-Field Theory

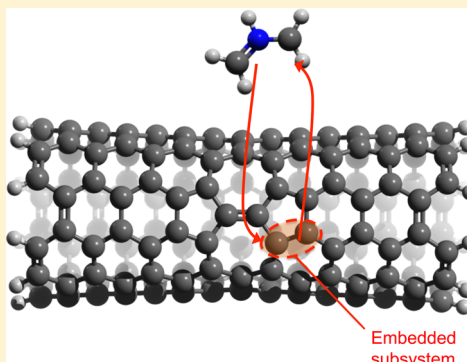
Mark E. Fornace,^{†,¶} Joonho Lee,^{†,¶} Kaito Miyamoto,^{‡,¶} Frederick R. Manby,^{*,‡} and Thomas F. Miller, III^{*,†}

[†]Division of Chemistry and Chemical Engineering, California Institute of Technology, Pasadena, California 91125, United States

[‡]Centre for Computational Chemistry, School of Chemistry, University of Bristol, Bristol BS8 1TS, United Kingdom

 Supporting Information

ABSTRACT: We introduce embedded mean-field theory (EMFT), an approach that flexibly allows for the embedding of one mean-field theory in another without the need to specify or fix the number of particles in each subsystem. EMFT is simple, is well-defined without recourse to parameters, and inherits the simple gradient theory of the parent mean-field theories. In this paper, we report extensive benchmarking of EMFT for the case where the subsystems are treated using different levels of Kohn–Sham theory, using PBE or B3LYP/6-31G* in the high-level subsystem and LDA/STO-3G in the low-level subsystem; we also investigate different levels of density fitting in the two subsystems. Over a wide range of chemical problems, we find EMFT to perform accurately and stably, smoothly converging to the high-level of theory as the active subsystem becomes larger. In most cases, the performance is at least as good as that of ONIOM, but the advantages of EMFT are highlighted by examples that involve partitions across multiple bonds or through aromatic systems and by examples that involve more complicated electronic structure. EMFT is simple and parameter free, and based on the tests provided here, it offers an appealing new approach to a multiscale electronic structure.



INTRODUCTION

Mean-field theories of electronic structure, including Kohn–Sham density-functional theory (KS-DFT)^{1,2} and density-functional tight-binding (DFTB),^{3–5} offer powerful approaches for condensed-phase simulations. The success of these methods rests upon their unique combination of generality, computational efficiency, and accuracy for a wide range of applications. The methods are general in the sense that they can produce an energy at a consistent level of theory for any configuration of any set of atoms, without the need for any further system-specific considerations. A range of compromises are available between accuracy and computational efficiency. Approximate hybrid DFT methods, such as B3LYP,⁶ offer very good accuracy for a range of chemical problems; but their computational cost severely limit length- and time scales in molecular dynamics simulations. Much more computationally efficient approaches are available, such as DFTB, but their efficiency comes at the price of reduced accuracy (and in some cases reduced generality).

Mitigating this trade-off between accuracy and efficiency, subsystem embedding has emerged as a powerful strategy for modeling the electronic structure of complex systems. In embedding methods, a high-level quantum-mechanical description of a chemically active subsystem is embedded in a surrounding environment described using a more approximate theory. The advantage of this approach is that it provides high accuracy for regions that demand it while avoiding the computational cost of a high-level calculation on the whole system. Notable examples of subsystem embedding include

QM/MM and ONIOM, although there are many other manifestations of the idea.^{7–22}

Despite their tremendous successes, QM/MM, ONIOM, and other widely used embedding schemes are not without problems that limit their applicability. In terms of generality, the way in which the partition is performed requires *a priori* knowledge of the chemical bonding, and the choice is limited by practical considerations. First, although it may be feasible to partition across an aliphatic C–C bond, it may be less straightforward for a conjugated or heteronuclear system. Second, the need to specify the fixed number of electrons per subsystem restricts the applicability of such methods to strongly insulating systems for which this number is unambiguous. Both of these issues are exacerbated in the description of chemical reactions for which the bonding connectivity (and electron number) may change as a function of nuclear coordinates. Some embedding theories, most notably density-matrix embedding theory¹⁹ and dynamical mean-field theory,²³ remove the need to fix subsystem particle numbers in the context of embedded correlated-wave function calculations; in this work, we present a new embedding theory that achieves a similar advantage in the context of embedded mean-field calculations.

In terms of accuracy, widely used embedding methods, such as QM/MM and ONIOM, involve approximations in the description of the subsystem partition that significantly impact

Received: December 6, 2014

Published: January 9, 2015

the overall accuracy of the calculation. QM/MM typically accounts for electrostatic interactions between subsystems through polarization of the QM region by MM point charges, while exchange-repulsion, dispersion, and other effects are approximated by simple empirical interaction potentials. For the case of ONIOM, a low-level calculation performed on the full system is corrected by the difference between high-level and low-level calculations performed on a subsystem, such that the interaction between subsystems is treated at the low level of theory.

Both approaches involve chemical termination of the subsystem that is treated at the higher level of theory, typically by introducing constructs such as link atoms^{24–30} or link orbitals^{31–39} to satisfy the valency of the atoms at the subsystem interface. Moreover, both approaches require the selection of a fixed electron number in the high-level subsystem, and neither allows changes in the number of electrons per subsystem as a function of the nuclear coordinates. These limitations present clear challenges for the description of processes where the chemical change cannot be localized to a small number of atoms.

In this paper, we describe embedded mean-field theory (EMFT), a subsystem embedding approach that addresses many of these challenges. By partitioning directly at the level of the atomic-orbital basis set, EMFT provides a mean-field description of the entire system that seamlessly combines different levels of theory for different subsets of atoms. There are no link atoms, link orbitals, geometry-dependent parameters or restrictions on particle number in subsystems, and full self-consistency between subsystems is achieved.

THEORY

The central idea of EMFT is to partition the basis set into subsets A and B, block the one-particle density matrix accordingly

$$\mathbf{D} = \begin{bmatrix} \mathbf{D}^{AA} & \mathbf{D}^{AB} \\ \hline \mathbf{D}^{BA} & \mathbf{D}^{BB} \end{bmatrix} \quad (1)$$

and compute the energy as a functional of \mathbf{D} with different levels of treatment for each sub-block. Given two different mean-field theories with energies

$$E_i[\mathbf{D}] = \text{tr } \mathbf{D}\mathbf{H}_0 + G_i[\mathbf{D}] \quad (2)$$

that differ only in the description of the two-electron terms (G_1 or G_2), the EMFT energy is obtained by minimizing

$$E[\mathbf{D}] = \text{tr } \mathbf{D}\mathbf{H}_0 + G_2[\mathbf{D}] + (G_1[\mathbf{D}^{AA}] - G_2[\mathbf{D}^{AA}]) \quad (3)$$

with respect to all elements of the density matrix \mathbf{D} . (Entirely analogous equations follow in the case where the two methods also differ in their core Hamiltonians).

This theory has a number of appealing properties, not least being its simplicity. EMFT is itself a mean-field theory with a Fock operator simply obtained by differentiation

$$F_{\alpha\beta} = \frac{\partial E[\mathbf{D}]}{\partial D_{\alpha\beta}}$$

and simple gradients with respect to nuclear displacements given by

$$\frac{\partial E[\mathbf{D}]}{\partial \mathbf{x}} = \text{tr } \mathbf{D}\mathbf{F}^{(x)} - \text{tr } \mathbf{W}\mathbf{S}^{(x)} \quad (4)$$

where \mathbf{W} is the energy-weighted density and $\mathbf{F}^{(x)}$ and $\mathbf{S}^{(x)}$ are the derivatives of the Fock and overlap matrices, respectively. Similarly, EMFT response theories, such as time-dependent EMFT (TD-EMFT), will be simple and straightforward.

Two additional advantages emerge from the fact that the number of electrons in each subsystem is determined directly from minimization of the EMFT energy. The first is that charge flow between the subsystems is naturally included, and the second is that there is no need for the user to specify *a priori* the number of electrons in each subsystem. Beyond the definition of the two mean-field theories and the list of atomic orbitals in each subsystem, there are no additional parameters.

Finally, we note that the individual subsystems in EMFT are treated as open quantum systems, such that the entanglement between them is fully included at the mean-field level. The EMFT framework is general, enabling the embedding of any mean-field theory in any other. Natural examples for the description of subsystem A might include hybrid,^{6,40} double-hybrid,⁴¹ or range-separated hybrid⁴² functionals; as well as self-consistent random-phase approximations.^{43,44} Subsystem B might be described by more computationally efficient DFT methods or DFTB.^{3–5}

In this work, we investigate the accuracy of the EMFT framework using KS-DFT with different exchange-correlation functionals for the two subsystems (i.e., GGA or hybrid functionals for subsystem A, and LDA^{45,46} for subsystem B). We also investigate the use of different basis sets for the two subsystems (e.g., minimal basis set in subsystem B), and finally, we investigate the use of different density-fitting basis sets for the two subsystems. This enables, for example, a B3LYP/6-31G*⁴⁷ treatment of subsystem A in an LDA/STO-3G^{48,49} treatment of subsystem B, at a fraction of the cost of the full B3LYP/6-31G* calculation on the whole system.

EMFT for Hybrid Functionals. In the case where the two mean-field theories are KS-DFT with different functionals, with possibly a hybrid functional for the high-level region, the energy expression is given by

$$\begin{aligned} E[\mathbf{D}] = & \text{tr } \mathbf{D}\mathbf{H}_0 + E_{J,2}[\mathbf{D}] + (E_{J,1}[\mathbf{D}^{AA}] - E_{J,2}[\mathbf{D}^{AA}]) \\ & + E_{xc,2}[\mathbf{D}] + (\mathbf{E}_{xc,1}[\mathbf{D}^{AA}] + \alpha \mathbf{E}_{EX}^A - \mathbf{E}_{xc,2}[\mathbf{D}^{AA}]) \end{aligned} \quad (5)$$

Here $E_{J,1}$ and $E_{J,2}$ are high- and low-level models for the Coulomb energy; $\mathbf{E}_{xc,1} + \alpha \mathbf{E}_{EX}^A$ is the (possibly hybrid) high-level exchange-correlation functional; and $E_{xc,2}$ is the low-level functional.

We have investigated two possible schemes for the treatment of exact exchange. In the simpler scheme, denoted EX0, the exact exchange in subsystem A is expressed

$$E_{EX0}^A = -\frac{1}{4} \sum_{\alpha\beta\gamma\delta \in A} D_{\alpha\beta}^{AA} (\alpha\gamma|\beta\delta) D_{\gamma\delta}^{AA}$$

This obviously implies great computational savings, reducing the unscreened cost of evaluating the exact exchange contribution by $O((N_A/N)^4)$, where N_A and N are measures of the size of subsystem A and of the whole system. For chemical processes that involve atoms close to the partition between subsystems, we have found that a second, slightly more complicated formalism performs more reliably. In this approach, labeled EX1, the exchange energy is computed as

$$E_{EX1}^A = -\frac{1}{4} \sum_{\alpha\beta \in A; \gamma\delta} D_{\alpha\beta}^{AA} (\alpha\gamma|\beta\delta) D_{\gamma\delta}^{AA} \quad (6)$$

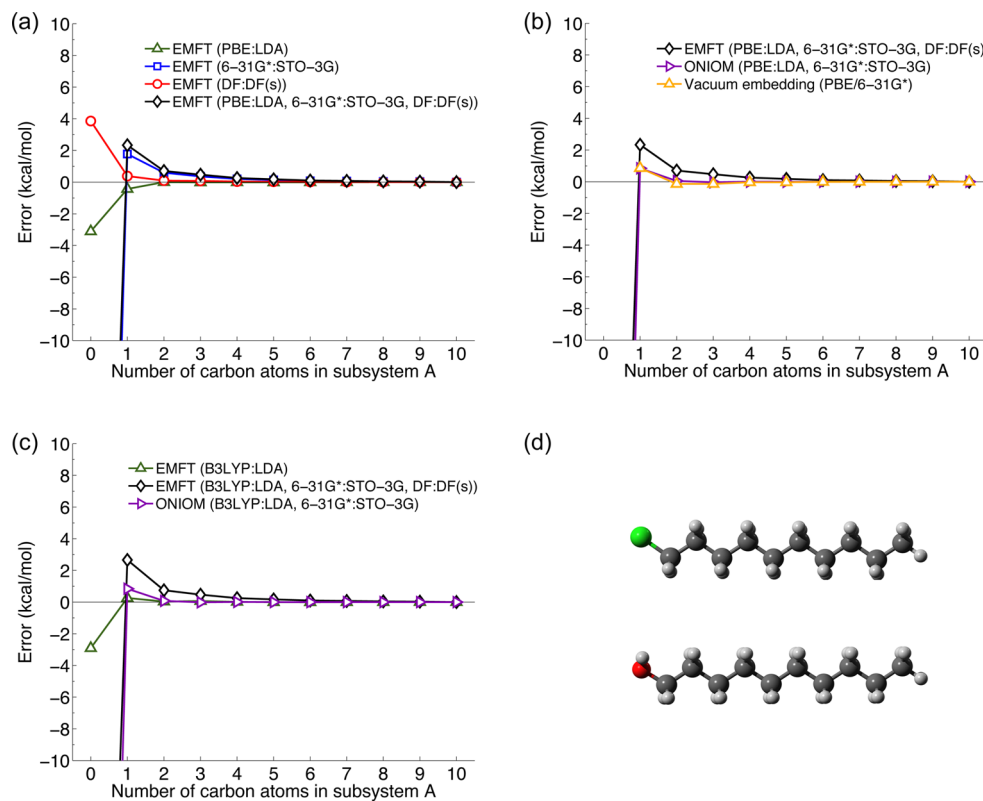


Figure 1. Embedding calculations for the 1-chlorodecane/1-decanol substitution reaction. (a) Error in the reaction energy as a function of the size of subsystem A for variants of EMFT. (b) Comparison of EMFT, ONIOM, and vacuum embedding for the error in the reaction energy. (c) Error in the EMFT reaction energy using a hybrid exchange-correlation functional in subsystem A. (d) Reactant and product structures. All errors are plotted relative to the reaction energy at the higher KS-DFT level of theory: -87.3 kcal/mol for panels (a) and (b) and -89.0 kcal/mol for panel (c). The reaction energy using the low-level (LDA/STO-3G/DF(s)) KS-DFT is -150.4 kcal/mol.

which includes additional couplings to subsystem B, and still offers a computational saving versus the full exchange evaluation of $O((N_A/N)^2)$. Throughout this study, numerical results for EMFT with hybrid functionals utilize the EX1 implementation of the exchange energy.

EMFT for Density Fitting. Equation 5 fully defines the EMFT approach to treating subsystems with different density-fitting basis sets,^{50–52} and density fitting for both the Coulomb^{53,54} and exchange⁵⁰ energy terms is used throughout this work. In terms of the standard density-fitting intermediate $B_K^{\alpha\beta} = [J^{-1/2}]_{KL}(L|\alpha\beta)$ where $J_{KL} = (K|L)$, the Coulomb energy contribution is thus

$$E_{J,2}[\mathbf{D}] + (E_{J,1}[\mathbf{D}^{AA}] - E_{J,2}[\mathbf{D}^{AA}]) \\ = \frac{1}{2} [D_{\alpha\beta} B_K^{\alpha\beta} B_K^{\gamma\delta} D_{\gamma\delta} + D_{\alpha\beta}^{AA} (B_K^{\alpha\beta} B_K^{\gamma\delta} - B_K^{\alpha\beta} B_K^{\gamma\delta}) D_{\gamma\delta}^{AA}]$$

where summation over repeated dummy indices is implied, and K and κ index large and small density-fitting auxiliary basis sets, respectively. In the limit of well-separated subsystems, this is equivalent to a standard density-fitting treatment of the Coulomb problem for the whole system, but with a large density-fitting basis on the atoms of subsystem A and a small fitting set in subsystem B. For interacting subsystems, these two approaches are no longer identical; however, they are closely related, and for simplicity of implementation, we adopt the latter in this work.

BENCHMARK TESTS

For a series of benchmark tests, we illustrate the performance of EMFT for implementations in which a higher-level KS-DFT approximation is used to describe part of the molecular system (subsystem A) and a lower-level KS-DFT approximation is used to describe the remainder of the system (subsystem B). The KS-DFT approximations for each subsystem vary with regard to three attributes: the atomic-orbital basis set, the exchange-correlation functional, and the density-fitting basis set used for all two-electron integrals. We use a notation for describing these EMFT calculations, such that any attribute that varies between the two subsystems is explicitly stated. For example, EMFT (6-31G*:STO-3G) refers to a calculation that uses the same exchange-correlation functional and the same density-fitting basis for both subsystems, while using the 6-31G* atomic orbital basis set for subsystem A and STO-3G for subsystem B. Similarly, EMFT (PBE:LDA, 6-31G*:STO-3G, DF:DF(s)) refers to a calculation in which all three attributes differ between the subsystems. In specifying the density-fitting basis sets, we use DF to indicate the Ahlrichs density-fitting basis^{51,52} for calculations in which PBE^{55,56} is the high-level exchange-correlation functional and to indicate cc-pVDZ/JKFIT⁵⁰ for calculations in which B3LYP⁶ is the high-level exchange-correlation functional; DF(s) indicates the subset of the corresponding fitting basis consisting of only the s-type functions. All EMFT calculations using the PBE functional in this section are performed using an in-house code, whereas all EMFT calculations using the B3LYP functional are performed using a modified version of the Molpro software package.^{57,58}

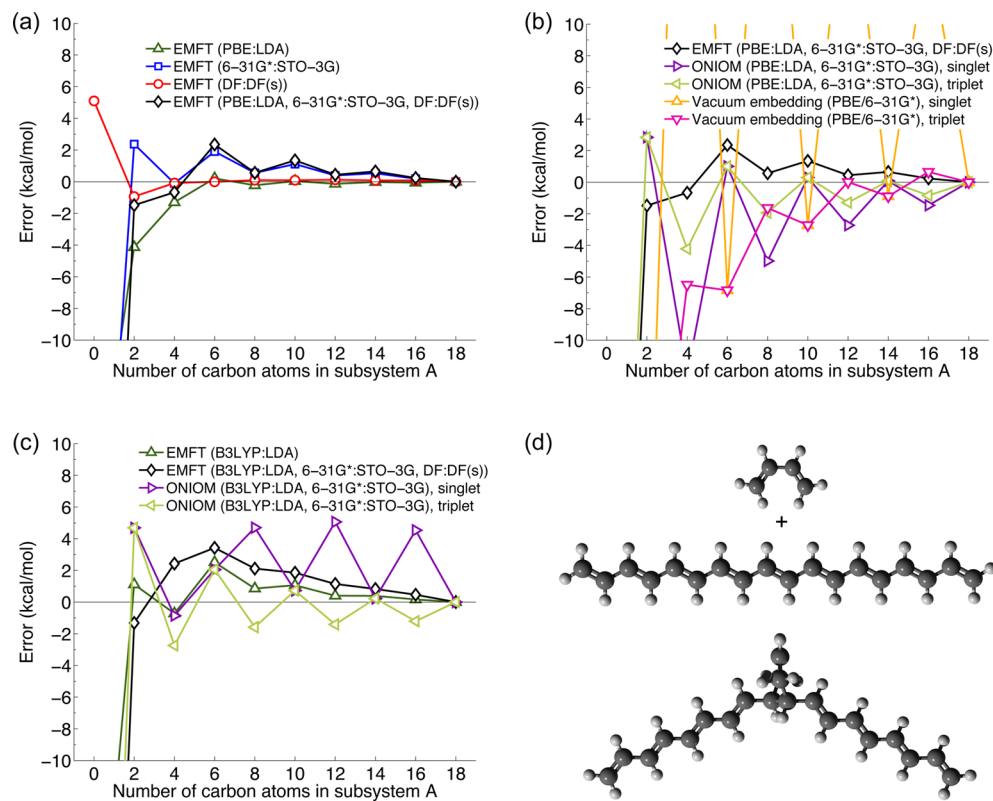


Figure 2. Embedding calculations for a Diels–Alder reaction involving an extended alkene chain. Results are presented as in Figure 1. All errors are plotted relative to the reaction energy at the higher KS-DFT level of theory: −26.7 kcal/mol for panels a and b and −21.0 kcal/mol for panel c. The reaction energy using the low-level (LDA/STO-3G/DF(s)) KS-DFT is −82.1 kcal/mol.

For comparison, we also provide results using the ONIOM method⁵⁹ with the subsystems treated using different levels of KS-DFT (denoted, for example, ONIOM (PBE:LDA, 6-31G*:STO-3G)). Additionally, we present results obtained using KS-DFT with vacuum embedding, such that subsystem A is simply terminated with link-atoms and interactions with subsystem B are neglected. Both the ONIOM and vacuum embedding calculations are implemented with H atoms terminating subsystem A, and for neither method is density fitting employed. For the ONIOM calculations, terminal H atoms are positioned according to the default parametrization scheme in Gaussian 09,^{59,60} and for the vacuum embedding calculations, the terminal H atom positions are optimized at the high-level theory with all other atom positions held fixed; EMFT involves no such parametrization or optimization, since it does not employ the explicit chemical termination of subsystem A. For cases in which the partition between subsystems involves splitting across two double bonds, the ONIOM and vacuum embedding calculations are performed using both singlet and triplet spin states of subsystem A;⁵⁹ again, we emphasize that no such designations or choices are needed for EMFT, which at no stage involves a separate calculation on a terminated version of either subsystem. All ONIOM and vacuum embedding calculations are performed using Gaussian 09.⁶⁰

Throughout this section, unless otherwise stated, figures that are plotted as a function of the number of carbon atoms in subsystem A assume that all noncarbon atoms attached to those carbon atoms are likewise included in subsystem A. We also use the convention that for the case in which zero carbon atoms are included in subsystem A, the result corresponds to treating all atoms with the low-level KS-DFT. Unless otherwise stated, data

are presented for molecular geometries that are optimized at the B3LYP/6-311G** level of theory.^{6,60–62}

Partitioning Across a Single Covalent Bond: A Simple Substitution Reaction. Results for the 1-chlorodecane/1-decanol substitution reaction are plotted in Figure 1. Errors in EMFT reaction energies using GGA and LDA functionals are presented in panel a, relative to the high-level KS-DFT result. It is clear that EMFT works well for this system, with the error for all variants becoming chemically negligible with only two carbon atoms included in subsystem A, despite the fact that the low-level (LDA/STO-3G/DF(s)) KS-DFT is in error by over 60 kcal/mol for this reaction. Comparison of the EMFT results indicates that the errors due to the difference in the subsystem atomic-orbital basis sets is significantly larger than errors due to the choice of exchange-correlation functional or density-fitting basis set, although all errors are small in this case.

In panel b, results obtained using EMFT, ONIOM, and vacuum embedding are compared. Like EMFT, both ONIOM and vacuum embedding work well for this example that involves simple partitioning across a single covalent bond.

Panel c reveals similar behavior for the implementation of EMFT using the hybrid exchange-correlation functional B3LYP in the EX1 approximation of eq 6. The accuracy of EMFT (B3LYP:LDA, 6-31G*:STO-3G, DF:DF(s)) is very similar to that of the corresponding GGA calculation. This result is notable, given that the EMFT (B3LYP:LDA, 6-31G*:STO-3G, DF:DF(s)) calculation involves approximations in both the exchange and Coulomb energy contributions associated with the mixed density-fitting basis, whereas the approximations associated with the mixed density-fitting basis appear only for

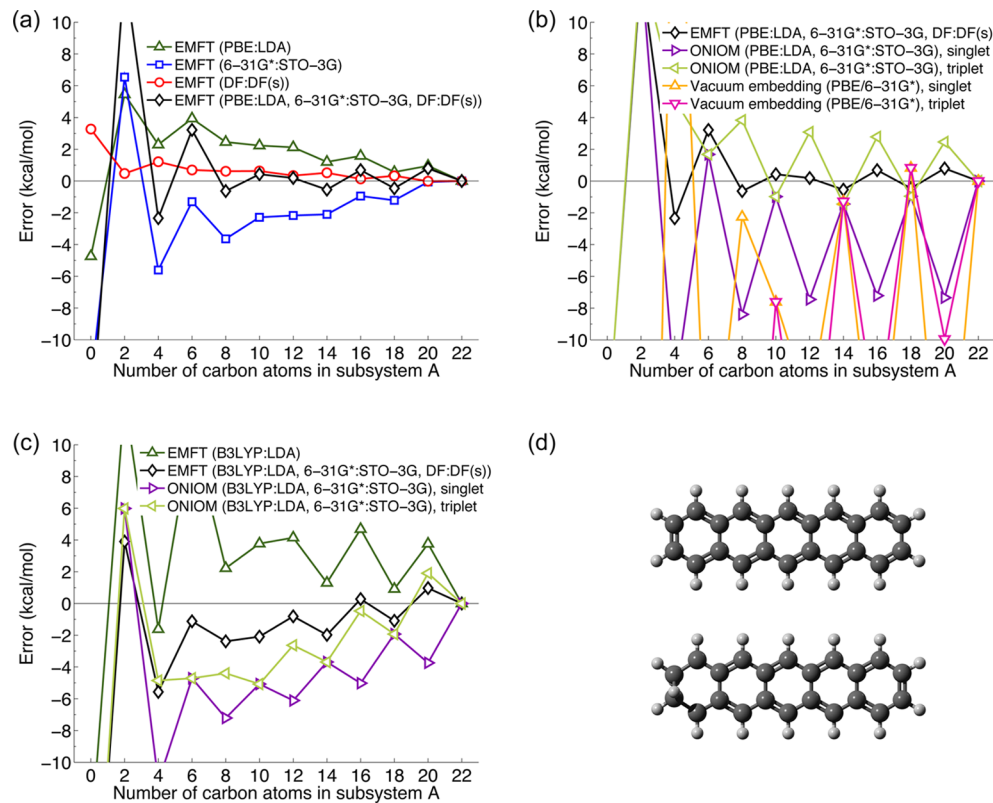


Figure 3. Embedding calculations for the terminal hydrogenation of pentacene. Results are presented as in Figure 1. All errors are plotted relative to the reaction energy at the higher KS-DFT level of theory: 22.6 kcal/mol for panels a and b and 32.7 kcal/mol for panel c. The reaction energy using the low-level (LDA/STO-3G/DF(s)) KS-DFT is 6.6 kcal/mol.

the Coulomb term in the EMFT (PBE:LDA, 6-31G*:STO-3G, DF:DF(s)) calculation.

Partitioning in a Conjugated System: The Diels–Alder Reaction.

Figure 2 presents results for a Diels–Alder reaction between the 1,3-butadiene and conjugated octadecanonaene hydrocarbons. To be clear, the *x*-axis in panels a–c indicates the number of carbon atoms from the octadecanonaene chain (panel d, top) that are included in subsystem A, starting with the two octadecanonaene carbon atoms to which the butadiene associates and increasing symmetrically toward the two ends of the octadecanonaene chain. For the case in which zero carbon atoms are included in subsystem A, all atoms in the reactant and product are treated at the lower level of theory, but for all other cases, the atoms associated with the butadiene reactant are included in subsystem A.

As is seen in panel a, EMFT performs well for this reaction, despite the fact that it involves partitioning across a conjugated system. The largest source of error in the EMFT results is again due to the use of different subsystem atomic-orbital basis sets, with errors due to the choice of the exchange-correlation functional and the density-fitting basis vanishing upon inclusion of only four carbon atoms in subsystem A. Panel b shows that both vacuum embedding and ONIOM exhibit significant errors for this reaction, which converge slowly with respect to the size of subsystem A and which exhibit substantial oscillations due to the changes in the bonds across which the subsystems are divided. Although the triplet implementations of these methods are consistently more accurate than the corresponding singlet implementations, it is clear that EMFT compares favorably with ONIOM and vacuum embedding, both in terms of accuracy and in terms of the simplicity of avoiding the need for a singlet/

triplet choice of spin-state. Finally, panel c illustrates the comparison of EMFT and ONIOM for hybrid functionals, the results of which are consistent with those seen for nonhybrid functionals in panel b. These results make clear that even for simple organic chemical reactions on relatively small systems, EMFT offers potential advantages in comparison to both ONIOM and vacuum embedding.

Partitioning in a Graphene-like System: Hydrogenation of Pentacene. Figure 3 presents results for the terminal hydrogenation reaction of pentacene, which is a more challenging case for embedding methods, because of the graphene-like conjugation of the reactants and products. The *x*-axis in panels a–c indicates the number of carbon atoms from pentacene that are included in subsystem A, starting with the two carbon atoms that are involved in the chemical transformation at one end of the pentacene molecule (panel d).

As is clear from panel a, EMFT again performs well for this system, converging quickly with respect to the size of subsystem A. Unlike the previous example, in which the only significant source of error came from the use of different subsystem atomic-orbital basis sets, this application of EMFT exhibits errors of similar magnitude from the use of different subsystem exchange-correlation functionals. It is interesting, however, that these basis-set and functional errors largely cancel in this example, such that errors in EMFT (PBE:LDA, 6-31G*:STO-3G, DF:DF(s)) become negligible with only eight carbon atoms in subsystem A.

In contrast to the EMFT results in panel a, panel b shows that the various ONIOM and vacuum embedding implementations exhibit significant errors for this reaction, and even more disturbingly, these large errors do not significantly decay with the size of subsystem A. This illustrates the fact that for systems in

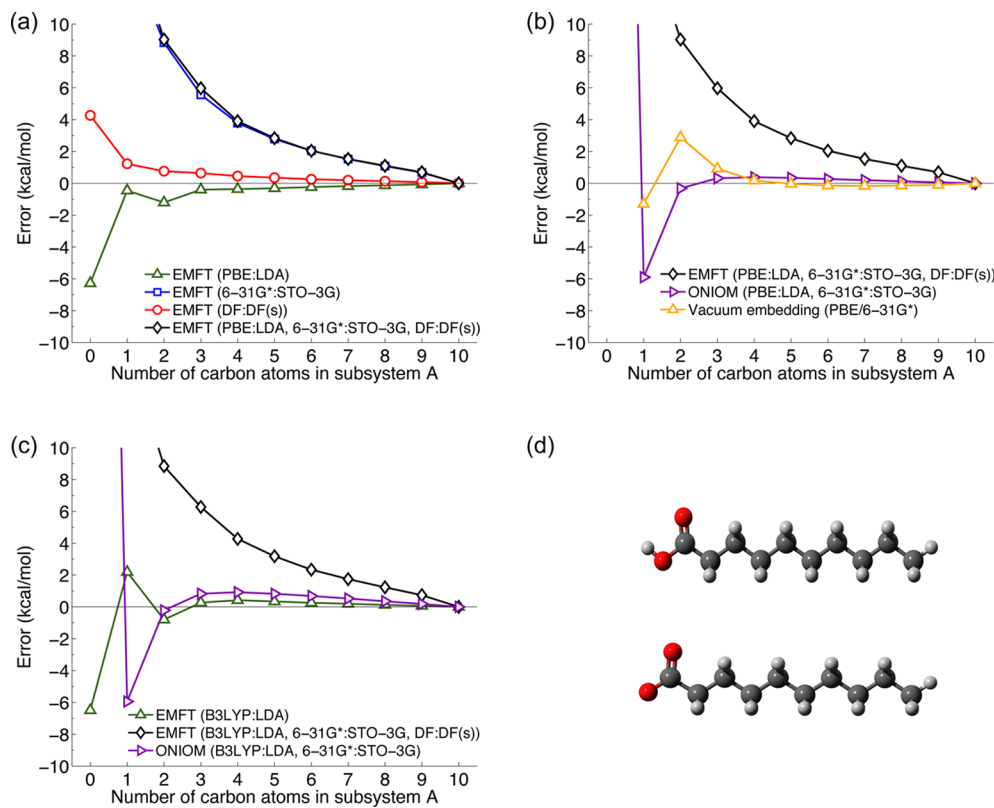


Figure 4. Embedding calculations for the deprotonation of decanoic acid. Results are presented as in Figure 1. All errors are plotted relative to the reaction energy at the higher KS-DFT level of theory: 363.1 kcal/mol for panels a and b and 363.4 kcal/mol for panel c. The reaction energy using the low-level (LDA/STO-3G/DF(s)) KS-DFT is 460.7 kcal/mol.

which there is no clear distinction between single and double bonds, the ONIOM method of subsystem partitioning will potentially incur well-known errors. The performance of EMFT using a hybrid functional (panel c) is comparable to the PBE results, but ONIOM with B3LYP is more accurate than ONIOM with PBE. Overall, errors in EMFT decay reasonably quickly for both choices of high-level functional, whereas with ONIOM this is only the case with one of them.

A Surprisingly Challenging Case: Deprotonation of a Terminal Carboxylic Acid. Figure 4 presents the error in the deprotonation energy of decanoic acid. Panel a clearly indicates that the largest error is from mixing bases. EMFT converges more slowly as compared to its behavior for the other reactions discussed above. The relative error, however, becomes less than 10% of its total reaction energy after including two carbons from the terminal. Panel b reveals that both vacuum embedding and ONIOM perform noticeably better than does EMFT. Because the reaction is strongly localized at the terminal carbon, even vacuum embedding, which has no interaction between subsystems, behaves well. Panel c shows similar trends.

It is found that the particularly poor behavior of EMFT in this case is consistent with errors seen in other reactions that manifest charges near the reaction centers. Mixing of two different bases while allowing the charge flow between subsystems inevitably leads to a spurious charge flow near the boundary. The effect of this unphysical charge flow becomes more obvious if the reaction accompanies a manifestation of charge, since it introduces an unphysical electrostatic interaction.

GEOMETRY OPTIMIZATIONS USING EMFT

An important feature of EMFT is the simplicity of its gradient theory (eq 4), which is essentially identical to that of KS-DFT. In this section, we demonstrate the accuracy of geometry optimizations performed using EMFT for the various benchmark reactants considered above. Geometry optimizations for EMFT are performed using an in-house code that employs G-DIIS,⁶³ BFGS update of the Hessian matrix,^{64–67} and RFO optimization.⁶⁸

Figure 5 presents results for which the reactants and products in each reaction are optimized as the size of subsystem A is varied. The figure presents the root-mean-square deviation (RMSD)⁶⁹ for the atoms in subsystem A, comparing optimized geometries from EMFT or ONIOM to the optimized geometries obtained from high-level KS-DFT. The EMFT results for the geometries of these systems are striking; in all four cases, the RMSD error for EMFT reduces to the expected accuracy of a high-level KS-DFT exchange-correlation functional (i.e., 0.02 Å) with less than four (and in most cases less than two) carbon atoms in subsystem A. In contrast, ONIOM exhibits substantially larger errors in panels (b–d), with the ONIOM results again illustrating sensitivity to the choice of treating subsystem A as either a singlet or triplet spin state. The singlet implementation of ONIOM is consistently much worse than that of EMFT, and for the pentacene reaction in panel c, both the singlet and triplet ONIOM results are significantly worse than that of EMFT. Although not presented, the reaction energy for each benchmark system, computed using the same level of theory for both the energy difference and for the optimized reactant and product geometries, are generally within 1 kcal/mol of the results presented in Figures 1 to 4.

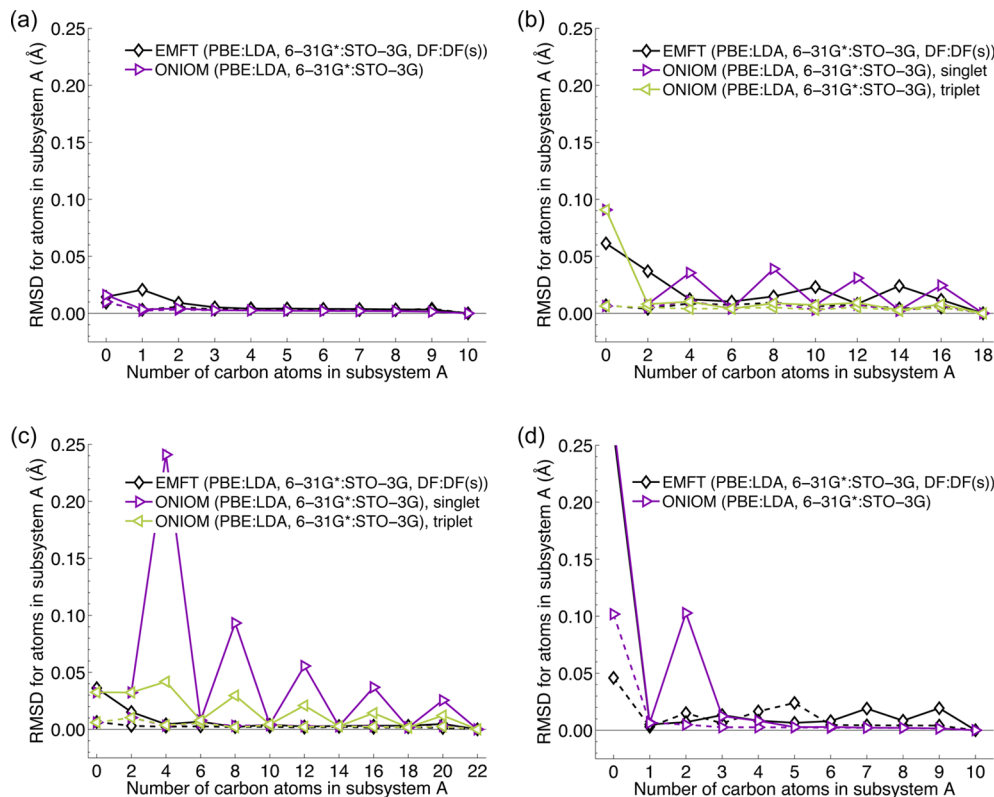


Figure 5. RMSD for the atoms in subsystem A, comparing optimized geometries from EMFT or ONIOM to the optimized geometries obtained from the higher-level KS-DFT. Results are obtained for the reactant and products of the four benchmark reactions, including (a) the 1-chlorodecane/1-decanol substitution reaction, (b) the Diels–Alder reaction, (c) the pentacene hydrogenation, and (d) the deprotonation of carboxylic acid. In all panels, the dashed lines correspond to reactants and the solid lines correspond to products.

■ PARTICLE NUMBER FLUCTUATIONS

As indicated above, a strength of the EMFT scheme is that it permits particle number fluctuations between subsystems and does not require the number of particles in either subsystem to be specified at any stage. As can be seen in the preceding results, EMFT is robust even when partitioning across multiple bonds and conjugated systems.

The standard deviation in particle number is computed from the KS determinant $|\Phi\rangle$ as

$$\sigma = [\langle \Phi | (\hat{n}^A)^2 | \Phi \rangle - \langle \Phi | \hat{n}^A | \Phi \rangle^2]^{1/2}$$

where \hat{n}^A is the number operator for the symmetrically orthogonalized atomic orbitals associated with subsystem A. In terms of the AA block of density matrix in the symmetrically orthogonalized atomic-orbital basis, this is given by $\sigma = [\text{tr } \mathbf{D}^{AA} - \text{tr}(\mathbf{D}^{AA})^2]^{1/2}$. Even with a mean-field wave function, the quantum state on some subset of the one-particle basis is typically entangled with its environment, and this can be measured through the von Neumann entropy measure $S = -\text{tr} \mathbf{D}^{AA} \ln_2 \mathbf{D}^{AA}$. Here, we use the \mathbf{D}^{AA} sub-block in the symmetrically orthogonalized AO basis, but this is expected to have little effect on the qualitative conclusions drawn here.

Both metrics are plotted in Figure 6 for neon dimer, ethane, ethene, and ethyne (as representative partitions across a nonbonding interaction and bond orders from one to three) as a function of the internuclear separation between the atoms that bridge the partition. All calculations are performed using PBE/6-31G*/DF KS-DFT. It can be seen that both measures increase considerably with increasing bond order, and in the case of single bonds, with decreasing internuclear separation. Moreover, the

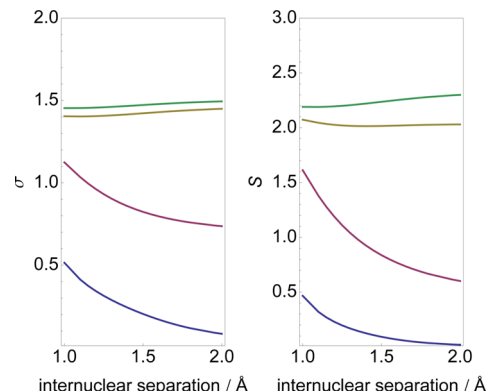


Figure 6. Variance in particle number (left panel) and the von Neumann entropy (right panel) in subsystems of neon dimer (blue), ethane (purple), ethene (gold), and ethyne (green), defined by symmetrically bisecting each system.

standard deviation in particle number is around 1 for cutting across the single bond, and 1.5 for double or triple bonds. This indicates that the choice in almost all embedding methods of fixed particle number in each subsystem is far from the physical situation, and emphasizes the advantage of EMFT in that it can capture these particle number fluctuations.

■ REPRESENTATIVE APPLICATIONS

Having systematically demonstrated EMFT for a range of benchmark systems, we now present applications of the method to more complex systems that are of interest from the recent computational chemistry literature. We present six additional

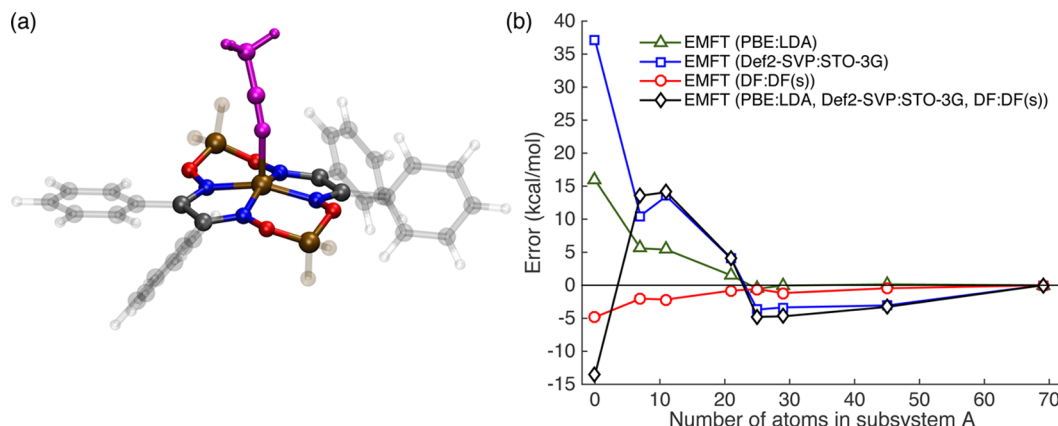


Figure 7. (a) Illustration of the binding reaction between acetonitrile (magenta) and Co catalyst complex (geometries from ref 71). For the choice of subsystem A with 21 atoms, the atoms associated with subsystem B are shown as translucent. (b) EMFT embedding errors, reported relative to the high-level (PBE/Def2-SVP/DF) KS-DFT reaction energy of 20.3 kcal/mol; the low-level (LDA/STO-3G/DF(s)) KS-DFT reaction energy is 6.7 kcal/mol.

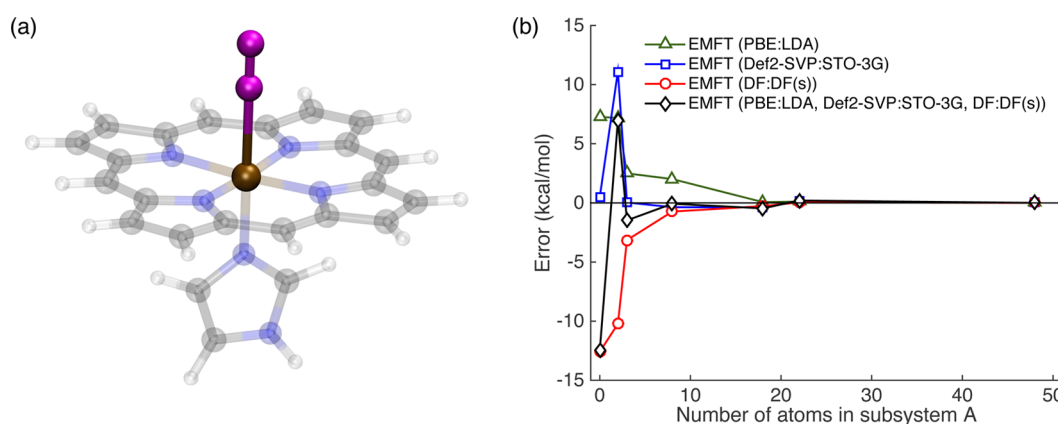


Figure 8. (a) Illustration of binding reaction between CO (magenta) and heme model complex (geometries from ref 75). For the choice of subsystem A with 3 atoms, the atoms associated with subsystem B are shown as translucent. (b) EMFT embedding errors, reported relative to the high-level (PBE/Def2-SVP/DF) KS-DFT reaction energy of 4.5 kcal/mol; the low-level (LDA/STO-3G/DF(s)) KS-DFT reaction energy is −8.5 kcal/mol.

applications, three of which correspond to ligand association reactions in transition-metal complexes and three of which correspond to defect formation in graphene sheets and carbon nanotubes. We present results that illustrate the convergence of errors in the EMFT with respect to high-level calculations performed over the full system, illustrating the utility of the method for realistic applications.

As before, in specifying the density-fitting basis sets, we use DF to indicate the Ahlrichs density-fitting basis for calculations in which PBE is the high-level exchange-correlation functional and to indicate cc-pVQZ/JKFIT for calculations in which B3LYP is the high-level exchange-correlation functional; DF(s) indicates the subset of the corresponding fitting basis consisting of only the s-type functions. Similarly, we use DF2 to indicate the Def2-SVP density fitting basis,⁷⁰ and DF2(s) denotes the subset that only contains s-type functions.

For each calculation reported in this section, the Supporting Information provides full details of the molecular geometries and the specific list of atoms that are included in subsystem A. For all plots that report errors as a function of the number of atoms in subsystem A, the case in which subsystem A includes zero atoms corresponds to treating the full system using the low-level KS-DFT. All EMFT calculations in this section are performed using a modified version of the Molpro software package, and all ONIOM calculations are performed using Gaussian 09.

LIGAND ASSOCIATION IN TRANSITION-METAL COMPLEXES

Acetonitrile Binding by a Cobalt-Based Hydrogen-Reduction Catalyst. Cobalt diglyoxime complexes have been recently researched as potential hydrogen reduction catalysts for artificial solar cells and other applications.^{72,73} Theoretical work in this area has focused on computing ligand-binding energies and reduction potentials associated with key steps in the catalytic process.^{71,74}

In particular, we examine the utility of EMFT in describing the binding of acetonitrile to the catalyst $\text{Co}^0(\text{dpgBF}_2)_2$ (dpg = diphenylglyoxime); Figure 7a illustrates the bound complex, with the acetonitrile ligand indicated in magenta. Dissociation of the axial acetonitrile ligand is thought to accompany catalyst reduction in some systems, playing an important part in the energetics of different reaction pathways.⁷⁴

Figure 7b presents EMFT (PBE:LDA, Def2-SVP:STO-3G, DF:DF(s)) results for the embedding of high-level KS-DFT in low-level KS-DFT. The convergence of error in the ligand binding energy is plotted with respect to the size of subsystem A. The atoms in subsystem A are included according to their proximity to the Co metal center, with the requirement that these atoms be contiguous via chemical bonds.

The binding energy for this reaction obtained using the high-level KS-DFT is 20.3 kcal/mol, and it is clear from Figure 7b that

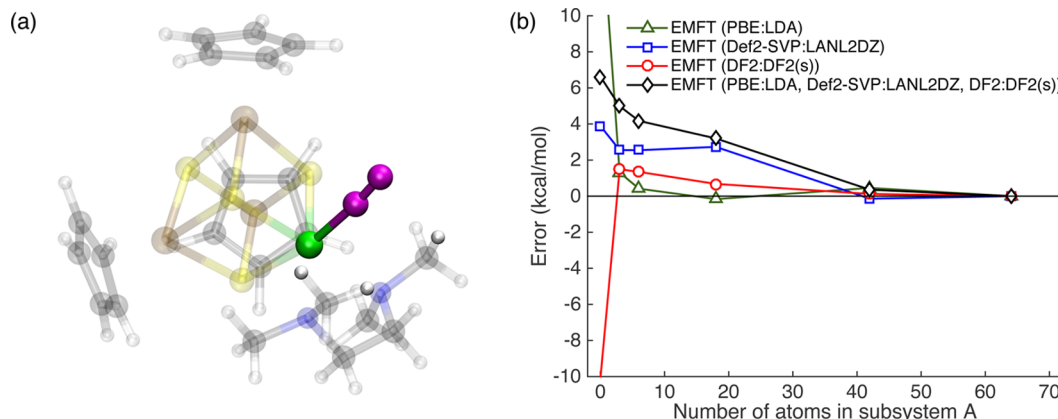


Figure 9. (a) Illustration of the binding reaction between N_2 (magenta) and RuIr₃S₄ cubane-type complex (geometries from ref 80). For the choice of subsystem A with six atoms, the atoms associated with subsystem B are shown as translucent. (b) EMFT embedding errors, reported relative to the high-level (PBE/Def2-SVP/DF2) KS-DFT reaction energy of 35.5 kcal/mol; the low-level (LDA/LANL2DZ/DF2(s)) KS-DFT reaction energy is 42.1 kcal/mol.

the various basis set and exchange-correlation functional approximations associated with the low-level KS-DFT lead to errors (−14 to 37 kcal/mol) that exceed the magnitude of the total binding energy. Nonetheless, EMFT leads to the systematic reduction of these errors with the increasing size of subsystem A, such that inclusion of only 21 atoms in subsystem A (illustrated in Figure 7a) leads to errors of less than 5 kcal/mol. As for the benchmark systems, it is clear from Figure 7b that the use of mixed atomic orbital basis sets leads to the largest source of error in the EMFT results.

CO Binding in an Iron–Porphyrin Complex. Heme binding of small molecules, such as CO, NO, and O₂, is a critical step in many bioinorganic processes.^{76,77} Theoretical approaches, including KS-DFT, have focused on clarifying the mechanism of these reactions, generally by using smaller model complexes for reasons of computational feasibility.^{78,79} Work using KS-DFT has also focused on benchmarking the accuracy of different functionals, the choice of which substantially affects computed results.⁷⁵ Here, we consider the binding energy between CO and a ferrous deoxy-heme model complex (deoxy-FeP(Im)) in the singlet spin state. Figure 8a illustrates the bound complex, with the CO ligand indicated using magenta and the O atom bonding with Fe.

Figure 8b presents EMFT (PBE:LDA, Def2-SVP:STO-3G, DF:DF(s)) results for the embedding of high-level KS-DFT in low-level KS-DFT. The convergence of error in the ligand binding energy is plotted with respect to the size of subsystem A. As for the previous example, the atoms in subsystem A are included according to their proximity to the transition metal center, with the requirement that these atoms be contiguous via chemical bonds.

The binding energy for this reaction obtained using the high-level KS-DFT is only 4.5 kcal/mol, but it is clear from Figure 8b that the various basis set and exchange-correlation functional approximations associated with the low-level KS-DFT lead to errors (−13 to 8 kcal/mol) that greatly exceed the magnitude of the total binding energy. EMFT again leads to the systematic reduction of these errors with the increasing size of subsystem A, such that inclusion of only three atoms in subsystem A (illustrated in Figure 8a) leads to errors of only 2 kcal/mol and larger subsystem sizes lead to even smaller errors.

N₂ Binding in a Cubane-Type RuIr₃S₄ Cluster. As a final inorganic example, we consider the binding of molecular

nitrogen to a mixed-metal Ru/Ir sulfido cluster, $[(\text{Cp}^*\text{Ir})_3\text{Ru}(\text{tmida})(\mu_3\text{-S})_4]$, (tmida = Me₂NCH₂NMe₂). Figure 9a illustrates the bound complex, with the N₂ ligand indicated using magenta. Molecular models of this type have been developed as functional analogues for the nitrogenase enzyme.⁸¹ In particular, the mixed-metal Ru/Ir sulfido cluster studied here has been shown to effectively bind N₂ and to exhibit substantial weakening of the N≡N bond in the bound complex.⁸² Previous KS-DFT studies have been employed to understand the energetics and structural features of the N₂ binding event.⁸⁰

Figure 9b presents EMFT (PBE:LDA, Def2-SVP:LANL2DZ, DF2:DF2(s)) results for the embedding of high-level KS-DFT in low-level KS-DFT. The Def2-SVP basis set includes effective core potentials (ECPs) for the Ir and Ru atoms,⁸³ and the LANL2DZ basis set includes ECPs for the Ir, Ru, and S atoms.^{84–87}

The convergence of error in the ligand binding energy is plotted with respect to the size of subsystem A. In this application, we determine the atoms in subsystem A using a simple radial distance cutoff measured from the binding nitrogen atom, regardless of whether this partitioning disrupts contiguous chemical bonds within the subsystems.

The binding energy for this reaction obtained using the high-level KS-DFT is 35.5 kcal/mol, and it is clear from Figure 9b that the various basis set and exchange-correlation functional approximations associated with the low-level KS-DFT lead to errors (ranging from roughly −10 to 16 kcal/mol) that are large in comparison to the magnitude of the total binding energy. EMFT again leads to the systematic reduction of these errors with the increasing size of subsystem A, such that inclusion of only six atoms in subsystem A (illustrated in Figure 9a) leads to a result that is within 12% of the high-level KS-DFT result for the binding energy. This result is particularly notable, given the complex electronic structure of the metal–sulfur cluster and given the fact that the subsystem partitioning was naively performed according to a simple distance cutoff. Further increasing the size of subsystem A in EMFT leads to the systematic further decrease of the error in the binding energy.

■ STONE–WALES DEFECTS IN GRAPHENE

The formation and propagation of Stone–Wales defects impact the mechanical, chemical, and physical properties of nanostructured carbon materials, such as graphene, fullerenes, and

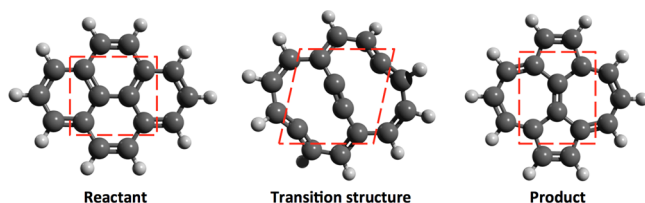


Figure 10. Reactant, transition structure, and product for Stone–Wales defect formation in $C_{16}H_{10}$. The dashed line indicates the atoms in subsystem A for the EMFT and ONIOM calculations.

Table 1. Activation and Reaction Energies for Stone–Wales Defect Formation in $C_{16}H_{10}$ ^a

method	activation energy	reaction energy
KS-DFT (B3LYP/6-31G*)	196.27	50.16
KS-DFT (LDA/STO-3G)	249.43 (53.16)	57.72 (7.56)
ONIOM (B3LYP:LDA, 6-31G*:STO-3G)	185.38 (-10.89)	56.27 (6.11)
EMFT (B3LYP:LDA, 6-31G*:STO-3G, DF:DF(s))	188.93 (-7.35)	49.67 (-0.49)

^aEnergies are reported in kcal/mol. Results in parentheses indicate the error relative to KS-DFT at the B3LYP/6-31G* level. KS-DFT are calculations performed using Gaussian 09.⁶⁰

carbon nanotubes.⁸⁸ Because of their tendency to enhance chemical reactivity,^{89,90} such defects may be functionalized to tune nanotube reactivities and solubilities or to separate out

defective nanotubes.⁹¹ Although numerous electronic structure studies have been performed,^{89–102} the investigation of Stone–Wales defects is hindered by the large system-sizes of realistic nanostructured carbon materials and the low number-density of the defects.⁹⁴ EMFT is potentially well-suited to the study of such systems, which we demonstrate via applications to a range of representative Stone–Wales defect processes.

All geometries in the following section are optimized using Gaussian 09⁶⁰ at the B3LYP/6-31G* level of theory, unless otherwise noted. As before, the ONIOM calculations involve termination of subsystem A using H atoms that are positioned according to the default parametrization scheme in Gaussian 09;^{59,60} all ONIOM calculations in this section treat subsystem A as a singlet spin state.

Defect Formation in a Small Graphene Sheet $C_{16}H_{10}$.

We first investigate the energetics of Stone–Wales defect formation in $C_{16}H_{10}$. Figure 10 presents the reactant, transition structure, and product associated with the defect formation. Table 1 presents results for the activation and reaction energies, obtained using KS-DFT, EMFT (B3LYP:LDA, 6-31G*:STO-3G, DF:DF(s)), and ONIOM (B3LYP:LDA, 6-31G*:STO-3G) calculations. The atoms associated with subsystem A in the EMFT and the ONIOM calculations are indicated in Figure 10.

As seen in Table 1, the low-level (LDA/STO-3G) KS-DFT differs significantly with respect to the high-level (B3LYP/6-31G*) KS-DFT for the description of defect formation, introducing errors of 53 and 8 kcal/mol for the activation and reaction energies, respectively. ONIOM improves the descrip-

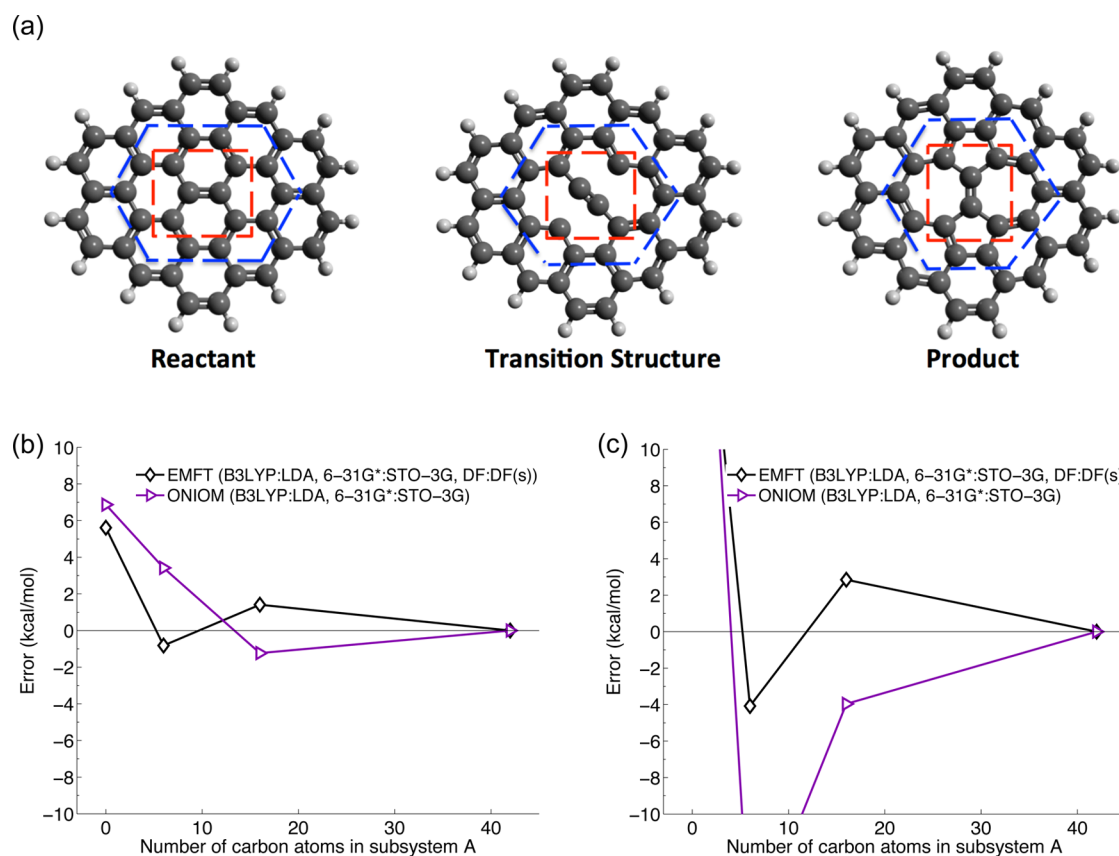


Figure 11. (a) Reactant, transition structure, and product for Stone–Wales defect formation in $C_{42}H_{16}$. (b) For the reaction energy, EMFT and ONIOM embedding errors are reported relative to the high-level (B3LYP/6-31G*) KS-DFT result of 72.3 kcal/mol; the low-level (LDA/STO-3G/DF(s)) KS-DFT result is 77.9 kcal/mol. (c) For the activation energy, EMFT and ONIOM embedding errors are reported relative to the high-level (B3LYP/6-31G*) KS-DFT result of 215.3 kcal/mol; the low-level (LDA/STO-3G/DF(s)) KS-DFT result is 242.5 kcal/mol.

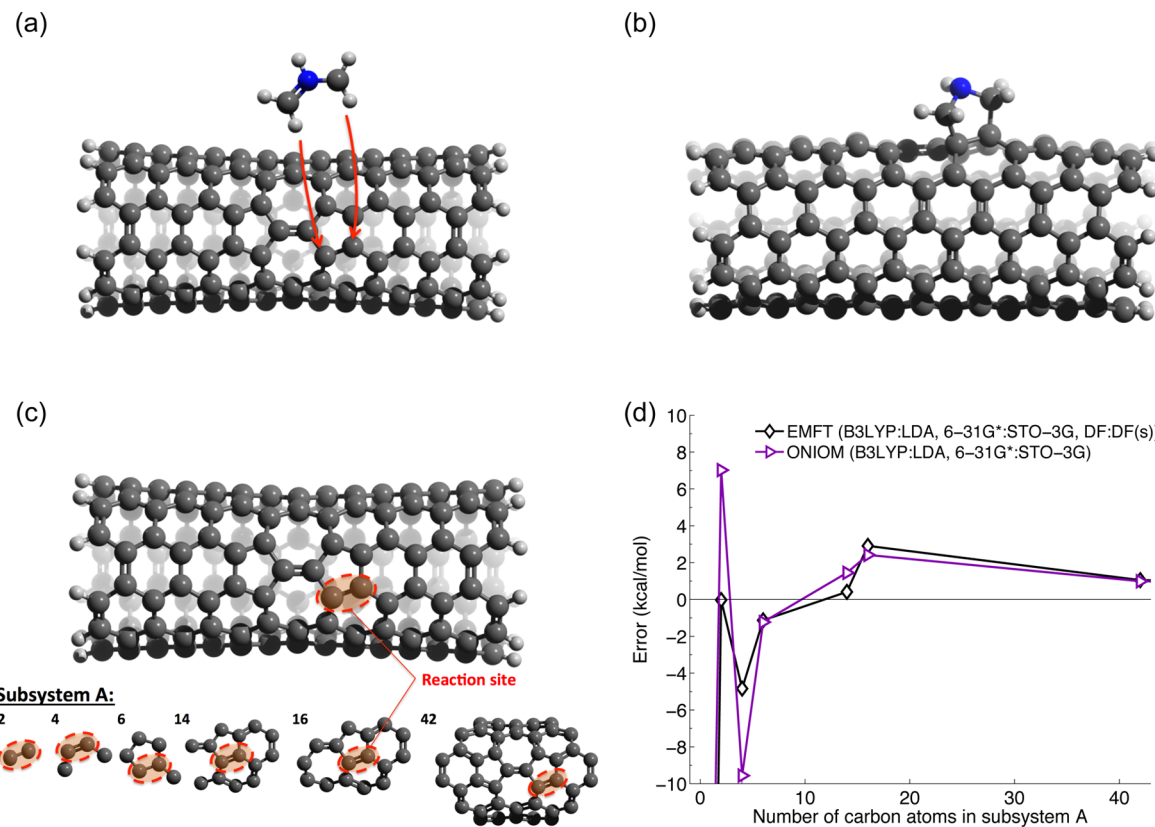


Figure 12. (a) Reactants and (b) product of the 1,3-dipolar cycloaddition of azomethine-ylide to a Stone–Wales defective carbon nanotube. (c) Illustration of the different choices for subsystem A that are considered. (d) EMFT and ONIOM embedding errors, reported relative to the high-level (B3LYP/6-31G*) KS-DFT reaction energy of -49.5 kcal/mol; the low-level (LDA/STO-3G/DF(s)) KS-DFT reaction energy is -122.3 kcal/mol.

tion of the transition process (reducing the error to with 11 kcal/mol), but it provides very little improvement in the reaction energy. It is clear that EMFT performs significantly better for this case, further reducing the error in the activation energy to approximately 7 kcal/mol (less than 4% of the total activation energy) and almost completely removing any error in the reaction energy. As observed earlier for the benchmark example of pentacene hydrogenation (Figure 3), EMFT is more accurate than ONIOM and provides greater simplicity by avoiding the need to specify the spin-state of the embedded subsystem.

Defect Formation in a Larger Graphene Sheet ($C_{42}H_{16}$). We next examine the formation of Stone–Wales defects in a larger graphene sheet (Figure 11a), computing the activation and reaction energies using KS-DFT and the embedding methods with two different sizes of subsystem A. As for the smaller graphene sheet, the low-level (LDA/STO-3G/DF(s)) KS-DFT differs significantly with respect to the high-level (B3LYP/6-31G*) KS-DFT for the description of defect formation, introducing errors of 5.6 and 27 kcal/mol for the reaction and activation energies, respectively.

As seen in Figure 11b and Figure 11c, EMFT provides a smaller error for the reaction and activation energies than ONIOM for the size of subsystem A. The distinction between methods is most pronounced for the smaller choice of subsystem A that includes only six atoms (indicated in red in Figure 11a). Even for this smaller subsystem, EMFT provides a reaction energy that is within 2 kcal/mol of the high-level KS-DFT result and an activation energy that is within 4 kcal/mol; for both of these quantities, ONIOM exhibits errors that are more than twice as large.

Cycloaddition of Azomethine-ylide to a Stone–Wales Defective Carbon Nanotube. In a final example, we consider the cycloaddition of azomethine-ylide at a Stone–Wales defect in a single-walled carbon nanotube ($C_{150}H_{20}$); Figure 12 panels a and b illustrate the reactant and product species, respectively. Previous studies have identified that the reaction proceeds most favorably at the five-member rings, as is highlighted in Figure 12(c).⁹¹ Using both EMFT (B3LYP:LDA, 6-31G*:STO-3G, DF:DF(s)) and ONIOM (B3LYP:LDA, 6-31G*:STO-3G) with subsystem A comprising the 42-carbon region shown in Figure 12c.

For this reaction, the low-level (LDA/STO-3G/DF(s)) KS-DFT predicts a reaction energy of -122.3 kcal/mol, which is over twice that obtained using the high-level (B3LYP/6-31G*) KS-DFT. Both EMFT and ONIOM significantly reduce this massive error (Figure 12d), although it is seen that EMFT is consistently more accurate, particularly for small sizes of subsystem A. Even for choices of subsystem A that include only two or four atoms from the nanotube in subsystem A, EMFT provides reaction energies that are within 10% of the high-level KS-DFT result; the ONIOM results for these subsystems exhibit errors that are at least twice as large. For larger subsystem sizes, the EMFT and ONIOM results are more similar.

CONCLUSIONS

In this paper we have introduced embedded mean-field theory (EMFT), a subsystem embedding approach that seamlessly combines different mean-field levels of theory for different subsystems into a mean-field description of the entire system.

The theory is notable for its simplicity, with respect to the calculation of energies, gradients, and other response properties. EMFT is also simple in terms of practical implementation, requiring only the convenient specification of subsystem partitioning at the level of the atomic-orbital basis and completely avoiding the use of link atoms, link orbitals, or any geometry-dependent parameters. Furthermore, EMFT avoids the need to specify the number of electron with each subsystem, thus allowing for the self-consistent flow of electron density between subsystems, as well as fluctuations in the number of electrons per subsystem. These features distinguish EMFT from other embedding schemes in which a separate calculation is performed on subsystem A, and we illustrate that particle-number fluctuations and entanglement at the mean-field level are a natural and important feature of describing conjugated systems.

We further demonstrate that EMFT is accurate across a diverse range of benchmark systems and more complex applications, including cases for which subsystem partitioning involves dividing across conjugated systems (such as graphene-like systems) or in transition metal complexes. In particular, we show that EMFT consistently performs well in comparison to ONIOM for both energies and optimized geometries, while avoiding the need to specify subsystem spin states or to introduce (and parametrize the position of) atoms that chemically terminate the subsystems.

Although we have only presented numerical results for one variant of EMFT, in which both subsystems are treated using KS-DFT, it is clear that alternative mean-field implementations will be worth exploring in the future. Nonetheless, the accuracy of the results presented here, as well as the fact that EMFT does not necessitate different partitioning choices at different geometries, suggests that the method is well-suited to the simulation of chemical dynamics.

The development of tools to enable dynamics simulations in complex systems that provide high-level KS-DFT accuracy for a small fraction of the cost is very much of interest, and we are enthusiastic about EMFT as a framework for pursuing this aim.

ASSOCIATED CONTENT

Supporting Information

Geometries in xyz format for all chemical systems presented in this paper, and details of embedding subsystems for transition-metal complexes. This material is available free of charge via the Internet at <http://pubs.acs.org>.

AUTHOR INFORMATION

Corresponding Authors

*E-mail: fred.manby@bris.ac.uk.

*E-mail: tfm@caltech.edu.

Author Contributions

[¶]M.E.F., J.L., and K.M. contributed equally to this work.

Funding

Some of this work was performed while F.R.M. was on sabbatical at Caltech; support for this visit was provided by the Institute for Advanced Study at the University of Bristol, and is gratefully acknowledged. Additionally, K.M. acknowledges the support of Toyota Central R&D Laboratories, Inc., J.L. acknowledges a

fellowship from the Kwanjeong Educational Foundation, and T.F.M. acknowledges support from a Camille and Henry Dreyfus Foundation Teacher-Scholar Award and an Alfred P. Sloan Foundation Research Fellowship.

Notes

The authors declare no competing financial interest.

REFERENCES

- (1) Kohn, W.; Sham, L. J. *Phys. Rev.* **1965**, *140*, A1133–A1138.
- (2) Parr, R. G.; Yang, W. *Density-Functional Theory of Atoms and Molecules*; Oxford Univ. Press: New York, 1989; pp 1–197.
- (3) Porezag, D.; Frauenheim, T.; Köhler, T.; Seifert, G.; Kaschner, R. *Phys. Rev. B* **1995**, *51*, 12947–12957.
- (4) Elstner, M.; Porezag, D.; Jungnickel, G.; Elsner, J.; Haugk, M. *Phys. Rev. B* **1998**, *58*, 7260–7268.
- (5) Gaus, M.; Cui, Q.; Elstner, M. *J. Chem. Theory Comput.* **2011**, *7*, 931–948.
- (6) Becke, A. D. *J. Chem. Phys.* **1993**, *98*, 1372–1377.
- (7) Wesolowski, T. A. *Computational Chemistry: Reviews of Current Trends*; World Scientific: Singapore, 2006; Vol. 10; pp 1–82.
- (8) Huang, P.; Carter, E. A. *Annu. Rev. Phys. Chem.* **2008**, *29*, 261–290.
- (9) Huang, C.; Carter, E. A. *J. Chem. Phys.* **2011**, *135*, 194104.
- (10) Elliott, P.; Cohen, M. H.; Wasserman, A.; Burke, K. *J. Chem. Theory Comput.* **2009**, *5*, 827–833.
- (11) Elliott, P.; Burke, K.; Cohen, M. H.; Wasserman, A. *Phys. Rev. A* **2010**, *82*, 024501.
- (12) Goodpaster, J. D.; Ananth, N.; Manby, F. R.; Miller, T. F. *J. Chem. Phys.* **2010**, *133*, 084103.
- (13) Goodpaster, J. D.; Barnes, T. A.; Miller, T. F. *J. Chem. Phys.* **2011**, *134*, 164108.
- (14) Goodpaster, J. D.; Barnes, T. A.; Manby, F. R.; Miller, T. F. *J. Chem. Phys.* **2012**, *137*, 224113.
- (15) Manby, F. R.; Stella, M.; Goodpaster, J. D.; Miller, T. F. *J. Chem. Theory Comput.* **2012**, *8*, 2564–2568.
- (16) Barnes, T. A.; Goodpaster, J. D.; Manby, F. R.; Miller, T. F. *J. Chem. Phys.* **2013**, *139*, 024103.
- (17) Goodpaster, J. D.; Barnes, T. A.; Manby, F. R.; Miller, T. F. *J. Chem. Phys.* **2014**, *140*, 18A507.
- (18) Gordon, M. S.; Fedorov, D. G.; Pruitt, S. R.; Slipchenko, L. V. *Chem. Rev.* **2012**, *112*, 632–672.
- (19) Knizia, G.; Chan, G. K. *Phys. Rev. Lett.* **2012**, *109*, 186404.
- (20) Jacob, C. R.; Neugebauer, J. *WIREs Comput. Mol. Sci.* **2014**, *4*, 325–362.
- (21) Neuhauser, D.; Baer, R.; Rabani, E. *J. Chem. Phys.* **2014**, *141*, 041102.
- (22) Knizia, G.; Chan, G. K.-L. Density matrix embedding: A strong-coupling quantum embedding theory. *J. Chem. Theory Comput.* **2013**, *9*, 1428–1432.
- (23) Georges, A.; Kotliar, G.; Krauth, W.; Rozenberg, M. *J. Rev. Mod. Phys.* **1996**, *68*, 13–125.
- (24) Field, M. J.; Bash, P. A.; Karplus, M. *J. Comput. Chem.* **1990**, *11*, 700–733.
- (25) Bakowies, D.; Thiel, W. *J. Phys. Chem.* **1996**, *100*, 10580–10594.
- (26) Zhang, Y.; Lee, T.; Yang, W. *J. Chem. Phys.* **1999**, *110*, 46.
- (27) Antes, I.; Thiel, W. *J. Phys. Chem. A* **1999**, *103*, 9290–9295.
- (28) Das, D.; Eurenius, K. P.; Billings, E. M.; Sherwood, P.; Chatfield, D. C.; Hodoscek, M.; Brooks, B. R. *J. Chem. Phys.* **2002**, *117*, 10534.
- (29) DiLabio, G. A.; Hurley, M. M.; Christiansen, P. A. *J. Chem. Phys.* **2002**, *116*, 9578.
- (30) Amara, P.; Field, M. *J. Theor. Chem. Acc.* **2003**, *109*, 43–52.
- (31) Ferenczy, G. G.; Rivail, J.; Surján, P. R.; Náray-Szabó, G. *J. Comput. Chem.* **1992**, *13*, 830–837.
- (32) Théry, V.; Rinaldi, D.; Rivail, J.; Maigret, B.; Ferenczy, G. G. *J. Comput. Chem.* **1994**, *15*, 269–282.
- (33) Assfeld, X.; Rivail, J. *Chem. Phys. Lett.* **1996**, *263*, 100–106.
- (34) Gao, J.; Amara, P.; Alhambra, C.; Field, M. *J. Phys. Chem. A* **1998**, *102*, 4714–4721.

- (35) Murphy, R. B.; Philipp, D. M.; Friesner, R. A. *J. Comput. Chem.* **2000**, *21*, 1442–1457.
- (36) Amara, P.; Field, M. J.; Alhambra, C.; Gao, J. *Theor. Chem. Acc.* **2000**, *104*, 336–343.
- (37) Pu, J.; Gao, J.; Truhlar, D. G. *J. Phys. Chem. A* **2004**, *108*, 632–650.
- (38) Jung, J.; Choi, C. H.; Sugita, Y.; Ten-no, S. *J. Chem. Phys.* **2007**, *127*, 204102.
- (39) Sun, Q.; Chan, G. K. L. *J. Chem. Theory Comput.* **2014**, *10*, 3784–3790.
- (40) Zhao, Y.; Truhlar, D. G. *Theor. Chem. Acc.* **2007**, *120*, 215–241.
- (41) Grimme, S. *J. Chem. Phys.* **2006**, *124*, 034108.
- (42) Yanai, T.; Tew, D. P.; Handy, N. C. *Chem. Phys. Lett.* **2004**, *393*, 51–57.
- (43) Furche, F. *Phys. Rev. B* **2001**, *64*, 195120.
- (44) Furche, F. *J. Chem. Phys.* **2008**, *129*, 114105.
- (45) Hohenberg, P.; Kohn, W. *Phys. Rev.* **1964**, *136*, B864.
- (46) Vosko, S. H.; Wilk, L.; Nusair, M. *Can. J. Phys.* **1980**, *58*, 1200.
- (47) Hehre, W. J.; Ditchfield, R.; Pople, J. A. *J. Chem. Phys.* **1972**, *56*, 2257.
- (48) Hehre, W. J.; Stewart, R. F.; Pople, J. A. *J. Chem. Phys.* **1969**, *51*, 2657.
- (49) Collins, J. B.; von Schleyer, P. R.; Binkley, J. S.; Pople, J. A. *J. Chem. Phys.* **1976**, *64*, 5142–5151.
- (50) Weigend, F. *Phys. Chem. Chem. Phys.* **2002**, *4*, 4285–4291.
- (51) Eichkorn, K.; Treutler, O.; Öhm, H.; Häser, M.; Ahlrichs, R. *Chem. Phys. Lett.* **1995**, *240*, 283–290.
- (52) Eichkorn, K.; Weigend, F.; Treutler, O.; Ahlrichs, R. *Theor. Chem. Acc.* **1997**, *97*, 119–124.
- (53) Vahtras, O.; Almlöf, J.; Feyereisen, M. *Chem. Phys. Lett.* **1993**, *213*, 514.
- (54) Dunlap, B. I. *Phys. Chem. Chem. Phys.* **2000**, *2*, 2113–2116.
- (55) Perdew, J. P.; Burke, K.; Ernzerhof, M. *Phys. Rev. Lett.* **1996**, *77*, 3865–3868.
- (56) Perdew, J. P.; Burke, K.; Ernzerhof, M. *Phys. Rev. Lett.* **1997**, *78*, 1396.
- (57) Werner, H.-J.; Knowles, P. J.; Knizia, G.; Manby, F. R.; Schütz, M. *WIREs Comput. Mol. Sci.* **2012**, *2*, 242–253.
- (58) Werner, H.-J.; Knowles, P. J.; Knizia, G.; Schütz, M.; Korona, T.; Lindh, R.; Mitrushenkov, A.; Rauhut, G.; Shamasundar, K. R.; Adler, T. B.; Amos, R. D.; Bernhardsson, A.; Berning, A.; Cooper, D. L.; Deegan, M. J. O.; Dobbyn, A. J.; Eckert, F.; Goll, E.; Hampel, C.; Hesselman, A.; Hetzer, G.; Hrenar, T.; Jansen, G.; Köpl, C.; Liu, Y.; Lloyd, A. W.; Mata, R. A.; May, A. J.; McNicholas, S. J.; Meyer, W.; Mura, M. E.; Nicklass, A.; O'Neill, D. P.; Palmieri, P.; Peng, D.; Pfleiderer, K.; Pitzer, R.; Reiher, M.; Shiozaki, T.; Stoll, H.; Stone, A. J.; Tarroni, R.; Thorsteinsson, T.; Wang, M. *MOLPRO*, version 2012.1, a package of ab initio programs; 2012. <http://www.molpro.net> (accessed Dec 1, 2014).
- (59) Dapprich, S.; Komáromi, I.; Byun, K.; Morokuma, K.; Frisch, M. J. *J. Mol. Struct. (Theochem.)* **1999**, *461*–462, 1–21.
- (60) Frisch, M. J.; Trucks, G. W.; Schlegel, H. B.; Scuseria, G. E.; Robb, M. A.; Cheeseman, J. R.; Scalmani, G.; Barone, V.; Mennucci, B.; Petersson, G. A.; Nakatsuji, H.; Caricato, M.; Li, X.; Hratchian, H. P.; Izmaylov, A. F.; Bloino, J.; Zheng, G.; Sonnenberg, J. L.; Hada, M.; Ehara, M.; Toyota, K.; Fukuda, R.; Hasegawa, J.; Ishida, M.; Nakajima, T.; Honda, Y.; Kitao, O.; Nakai, H.; Vreven, T.; Montgomery, J. A., Jr.; Peralta, J. E.; Ogliaro, F.; Bearpark, M.; Heyd, J. J.; Brothers, E.; Kudin, K. N.; Staroverov, V. N.; Kobayashi, R.; Normand, J.; Raghavachari, K.; Rendell, A.; Burant, J. C.; Iyengar, S. S.; Tomasi, J.; Cossi, M.; Rega, N.; Millam, J. M.; Klene, M.; Knox, J. E.; Cross, J. B.; Bakken, V.; Adamo, C.; Jaramillo, J.; Gomperts, R.; Stratmann, R. E.; Yazyev, O.; Austin, A. J.; Cammi, R.; Pomelli, C.; Ochterski, J. W.; Martin, R. L.; Morokuma, K.; Zakrzewski, V. G.; Voth, G. A.; Salvador, P.; Dannenberg, J. J.; Dapprich, S.; Daniels, A. D.; Farkas, Ö.; Foresman, J. B.; Ortiz, J. V.; Cioslowski, J.; Fox, D. J. *Gaussian 09*, revision D.01; Gaussian Inc.: Wallingford CT, 2009.
- (61) Krishnan, R.; Binkley, J. S.; Seeger, R.; Pople, J. A. *J. Chem. Phys.* **1980**, *72*, 650–654.
- (62) Li, X.; Frisch, M. J. *J. Chem. Theory Comput.* **2006**, *2*, 835–839.
- (63) Császár, P.; Pulay, P. *J. Mol. Struct.* **1984**, *114*, 31–34.
- (64) Broyden, C. G. *IMA J. Appl. Math.* **1970**, *6*, 222–231.
- (65) Fletcher, R. *Comput. J.* **1970**, *13*, 317.
- (66) Goldfarb, D. *Math. Comput.* **1970**, *24*, 23–26.
- (67) Shanno, D. F. *Math. Comput.* **1970**, *24*, 647–656.
- (68) Banerjee, A.; Adams, N.; Simons, J.; Shepard, R. *J. Phys. Chem.* **1985**, *89*, 52–57.
- (69) Kabsch, W. *Acta Crystallogr., Sect. A* **1976**, *32*, 922–923.
- (70) Weigend, F. *Phys. Chem. Chem. Phys.* **2006**, *8*, 1057–1065.
- (71) Solis, B. H.; Hammes-Schiffer, S. *J. Am. Chem. Soc.* **2011**, *133*, 19036–9.
- (72) Hu, X.; Cossart, B. M.; Brunschwig, B. S.; Lewis, N. S.; Peters, J. C. *Chem. Commun.* **2005**, *1*, 4723–4725.
- (73) Hu, X.; Brunschwig, B. S.; Peters, J. C. *J. Am. Chem. Soc.* **2007**, *129*, 8988–8998.
- (74) Solis, B. H.; Hammes-Schiffer, S. *Inorg. Chem.* **2011**, *50*, 11252–62.
- (75) Strickland, N.; Harvey, J. *J. Phys. Chem. B* **2007**, *111*, 841–852.
- (76) Collman, J.; Brauman, J. *Proc. Natl. Acad. Sci. U.S.A.* **1976**, *73*, 3333–3337.
- (77) Kachalova, G. S. *Science* **1999**, *284*, 473–476.
- (78) Harvey, J. *J. Am. Chem. Soc.* **2000**, *122*, 12401–12402.
- (79) Spiro, T.; Zgierski, M.; Kozlowski, P. *Coord. Chem. Rev.* **2001**, *221*, 923–936.
- (80) Tanaka, H.; Mori, H.; Seino, H.; Hidai, M. *J. Am. Chem. Soc.* **2008**, *130*, 9037–9047.
- (81) Hidai, M.; Mizobe, Y. *Can. J. Chem.* **2005**, *83*, 358–374.
- (82) Mori, H.; Seino, H.; Hidai, M.; Mizobe, Y. *Angew. Chem., Int. Ed.* **2007**, *46*, 5431–5434.
- (83) Weigend, F.; Ahlrichs, R. *Phys. Chem. Chem. Phys.* **2005**, *7*, 3297–3305.
- (84) Wadt, W. R.; Hay, P. J. *J. Chem. Phys.* **1985**, *82*, 284.
- (85) Hay, P. J.; Wadt, W. R. *J. Chem. Phys.* **1985**, *82*, 270.
- (86) Hay, P. J.; Wadt, W. R. *J. Chem. Phys.* **1985**, *82*, 299.
- (87) Dunning, T. H.; Hay, J. P.; Schaefer, H. F. *Methods of Electronic Structure Theory*; Springer: US, 1977; pp 1–462.
- (88) Stone, A. J.; Wales, D. J. *Chem. Phys. Lett.* **1986**, *128*, 501.
- (89) Dinadyalane, T. C.; Murray, J. S.; Concha, M. C.; Politzer, P.; Leszczynski, J. *J. Chem. Theory Comput.* **2010**, *6*, 1351.
- (90) Boukhvalov, D. W.; Katsnelson, M. I. *Nano Lett.* **2008**, *8*, 4373.
- (91) Yang, T.; Zhao, X.; Nagase, S. *J. Comput. Chem.* **2013**, *34*, 2223.
- (92) Kang, J.; Bang, J.; Ryu, B.; Chang, K. *J. Phys. Rev. B* **2008**, *77*, 115453.
- (93) Ma, J.; Alfè, D.; Michaelides, A.; Wang, E. *Phys. Rev. B* **2009**, *80*, 033407.
- (94) Eggen, B. R.; Heggie, M. I.; Jungnickel, G.; Latham, C. D.; Jones, R.; Briddon, P. R. *Science* **1996**, *272*, 87.
- (95) Nardelli, M. B.; Yakobson, B. I.; Bernholc, J. *Phys. Rev. B* **1998**, *57*, R4277.
- (96) Nardelli, M. B.; Yakobson, B. I.; Bernholc, J. *Phys. Rev. Lett.* **1998**, *81*, 4656.
- (97) Samsonidze, G. G.; Samsonidze, G. G.; Yakobson, B. I. *Phys. Rev. Lett.* **2002**, *88*, 065501.
- (98) Dinadyalane, T. C.; Leszczynski, J. *Chem. Phys. Lett.* **2007**, *434*, 86.
- (99) Zurek, E.; Pickard, C. J.; Autschbach, J. *J. Phys. Chem. C* **2008**, *112*, 11744.
- (100) Page, A. J.; Ohta, Y.; Okamoto, Y.; Irle, S.; Morokuma, K. *J. Phys. Chem. C* **2009**, *113*, 20198.
- (101) Ewels, C. P.; Heggie, M. I.; Briddon, P. R. *Chem. Phys. Lett.* **2002**, *351*, 178.
- (102) Carlsson, J. M.; Scheffler, M. *Phys. Rev. Lett.* **2006**, *96*, 046806.